

Micelles via self-assembly of amphiphilic beta-cyclodextrin block copolymers as drug carrier for cancer therapy

Xiufang Li, Hui Liu, Jianbing Li, Zhiwei Deng, Lingjun Li, Junjun Liu, Jing Yuan, Peiru Gao, Yanjing Yang*, Shian Zhong*

School of Chemistry and Chemical Engineering, Central South University, Changsha 410083, China

ARTICLE INFO

Keywords:

Amphiphilic β -CD
Block copolymer
Drug carrier
Reductive stimulus responsive
Drug loading capacity

ABSTRACT

We developed intelligent, star-shaped amphiphilic β -cyclodextrin (β -CD) co-polymer nanocarriers to circumvent the poor drug loading and water-solubility of β -CD. The secondary hydroxyl groups of β -CD were methylated to improve solubility, and the primary hydroxyl groups were conjugated with mPEG-b-PCL-SH through disulfide linkage to amplify the hydrophobic cavity and enhance the stability of the nanocarrier. A series of amphiphilic β -CD block copolymers (CCPPs) differing in molecular weights were synthesized that could self-assemble into core-shell nanospheres measuring 50–70 nm in water. The different CCPP carriers were screened for their drug loading, encapsulation and release efficiencies, and CCPP-2 showed the highest drug loading capacity of 31.9% by weight. These nanocarriers accumulated at the tumor site through the EPR effect and released the drug in a controlled manner in the reductive tumor microenvironment, with negligible premature leakage and side effects. Therefore, CCPP-2 shows significant potential as a smart and efficient nanovehicle for anticancer drug delivery.

1. Introduction

Cancer remains a major cause of morbidity and mortality worldwide despite advances in therapeutic modalities [1]. Most malignancies still rely on conventional chemotherapy, which however is limited by the poor water solubility, non-selective *in vivo* distribution, severe systemic side effects [2], and premature leakage [3,4] of the drugs. Therefore, it is necessary to design intelligent drug delivery system (IDDS) to circumvent the above limitations and improve the treatment outcome in cancer patients. Amphiphilic block polymeric micelles have gained considerable attention as nano-scale drug-delivery systems for myriad clinical applications due to their ability to enhance the uptake of poorly water-soluble drugs, achieve sustained drug release, and specifically target tumor tissues [5–9]. However, studies have reported low doxorubicin (DOX) loading capacities (< 10%) of simple amphiphilic block copolymers like PEG-b-PCL, PEG-b-PLA and PEG-b-PCL-b-PEG [10–14]. The loading capacity was also not significantly improved in the new generation star-shaped amphiphilic copolymers containing poly-amidoamine dendrimer cores and PEG-b-PCL arms [15]. Beta-cyclodextrins (β -CD) are native cyclic oligomers composed of seven glucopyranose units linked by α -1, 4-glycosidic bonds, and have a hydrophilic exterior and hydrophobic interior [16] giving them the appearance of hollow, truncated cones. The hydrophobic cavity of β -CD

has been extensively utilized to construct drug carriers [17], and DOX loaded into β -CD exhibits a stronger anti-proliferative effect compared to free DOX due to higher cellular uptake [18,19]. However, β -CD has limited clinical utility due to poor water solubility and sub-optimal drug-loading capacity [20]. The former can be attributed to the formation of strong intermolecular hydrogen bonds between β -CD units that reduces hydrogen bonding with water molecules. Therefore, several chemically modified β -CDs such as methylated β -CDs [21], hydroxyalkylated β -CDs [22] and ionic β -CDs [23], have been synthesized that have improved water solubility on account of the disrupted intermolecular hydrogen bonds between the secondary hydroxyl groups of parent β -CDs. However, enhanced water solubility of these copolymers does not necessarily lead to higher drug-loading capacity, which can only be substantially augmented by increasing the volume of the hydrophobic cavity. Therefore, micelles self-assembled from amphiphilic β -CD-based polymers have been designed, which offer several advantages compared to the parent β -CDs like larger core-shell structure, tunable physicochemical properties, prolonged blood circulation [24,25], high water solubility and the ability to solubilize hydrophobic drugs [26], high drug loading capacity and high encapsulation efficiency. Qiu et al. [27] designed star-like PLA-b-PEG copolymers-based nanosystems using the β -CD core, which exhibited enhanced stability and increased drug loading capacity. Xiao et al. [28] also used a β -CD-

* Corresponding authors.

E-mail addresses: yangyanjing@csu.edu.cn (Y. Yang), zhongshian@aliyun.com (S. Zhong).

<https://doi.org/10.1016/j.colsurfb.2019.110425>

Received 5 May 2019; Received in revised form 16 July 2019; Accepted 3 August 2019

Available online 08 August 2019

0927-7765/ © 2019 Elsevier B.V. All rights reserved.

based initiator to construct cationic star polymers with 21ACSPs arms that demonstrated excellent biocompatibility. Therefore, the drug loading capacity of β -CD can be significantly enhanced by combining it with a block copolymer. Stimuli-responsive anti-cancer drug delivery systems that can specifically release the cargo at the tumor in response to the low pH [29,30], redox imbalance [31,32] and temperature [33,34] of the tumor microenvironment have gained considerable attention in recent years. These unique stimuli can be utilized to trigger the release of chemotherapeutic agents into the tumor cells while avoiding drug leakage into healthy cells. Therefore, the β -CD-block copolymer drug carriers also need to possess stimulus-responsive bonds in order to achieve targeted enrichment and release of the chemotherapeutic agents.

We developed a novel amphiphilic star-like reductive stimulus-responsive drug carrier using β -CD core and polyethylene glycol (PEG)/polycaprolactone (PCL) arms. The primary hydroxyl groups of β -CD were conjugated to the PEG-PCL blocks and hydrosulphonyls, and the secondary hydroxyl groups were chemically modified with iodomethane. The methyl groups and PCL acted as the hydrophobic core and PEG served as the hydrophilic shell, and the cavity resulting from the self-assembly of the amphiphilic β -CD block copolymers (CCPP) into core-shell nanospheres provided sufficient space for DOX. CCPP-2 showed high drug loading capacity of 31.9%, in addition to rapid but targeted drug release under reductive stimulus. The amphiphilic drug carrier also showed enhanced anti-tumor effect and low systemic toxicity in a tumor-bearing mouse model. The overall procedure for the synthesis of amphiphilic drug carrier combined with reduction-triggered drug release was designed for drug delivery to tumor tissues (Scheme 1).

2. Materials and methods

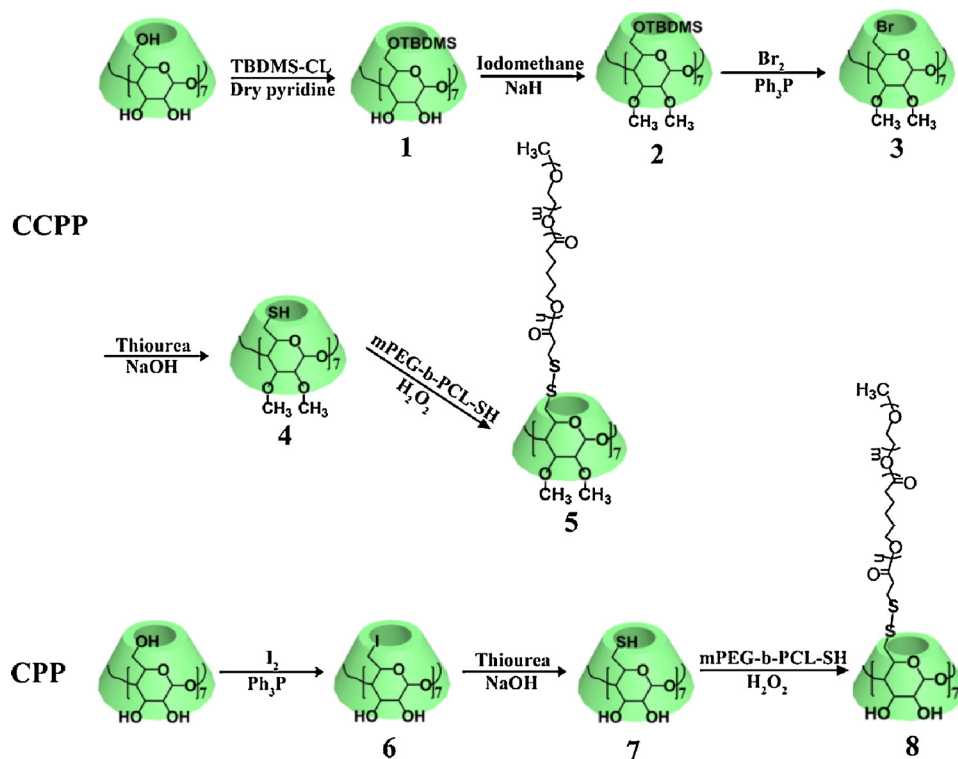
2.1. Reagents

β -CD, triphenylphosphine (PPh_3), thiourea, I_2 , ϵ -Caprolactone,

stannous octoate, 3,3'-thiodipropionic acid (DTPA), N,N'-dicyclohexylcarbodiimide (DCC), tertbutyldimethylsilyl chloride (TBDMS-Cl), bromine (Br_2) and 4-dimethylaminopyridine (DMAP) were obtained from Energy Chemical Technology Co., Ltd. (Shanghai, China). Sodium methoxide was purchased from Maya Reagent Company (Zhejiang, China), methoxypolyethylene glycols (MPEG; M_w : 2000) was purchased from Sinopharm Chemical Reagent Co. Ltd, 4', 6-Diamidino-2-phenylindole (DAPI) from Molecular Probes (USA), and 1, 1'-Dioctadecyl-3, 3, 3', 3'-tetramethyl indotricarbocyanine iodide (Dir) from Biotium Company (USA). DL-Dithiothreitol (DTT), sodium hydride (NaH), iodomethane (CH_3I), coumarin-6 (C6) and DOX were obtained from Aladdin Chemical Company (Shanghai, China). Fetal bovine serum (FBS), Dulbecco's modified eagle medium (DMEM) and RPMI 1640 medium were purchased from Biological Industries (Israel), and penicillin/streptomycin and 0.25% Trypsin-EDTA from Invitrogen (USA). Cell Counting Kit-8 (CCK-8) was procured from Shanghai Seven Seas Biotechnology Co. Ltd. All reagents and solvents were of analytical purity. The water used for all experiments was doubly distilled.

2.2. Synthesis and characterization of CCPP

The three-step synthesis of 2,3- CH_3O - β -CD-(s-s-PCL-b-mPEG) $_7$ or CCPP is outlined in Fig. 1. A series of thiol-terminated mPEG-b-PCL copolymers incorporating PCL blocks of different molecular weights (M_w) were first synthesized by ring-opening polymerization of ϵ -caprolactone with mono-hydroxyl-terminated mPEG initiator and stannous octoate catalyst, followed by sequential esterification and 1,4-dithio-threitol (DTT) reduction (Fig. S1). The β -cyclodextrin derivative per-6-SH-2,3-O CH_3 - β -CD was then synthesized by methylating the secondary hydroxyls and mercaptoylating the primary hydroxyls through four-step affinity substitution reactions (Fig. 1). Finally, the thiol-terminated mPEG-b-PCL were conjugated to the -SH groups of per-6-SH-2,3-O CH_3 - β -CD by H_2O_2 -mediated oxidation (Fig. 1) to obtain CCPP. As a control, the non-methylated β -CD-(s-s-PCL-b-mPEG) $_7$ or CPP was also synthesized using the same methods. The respective co-



Scheme 1. Schematic illustration of (A) self-assembly of the amphiphilic β -CD block copolymer micelle; (B) the mechanism of anticancer drug vehicles in tumor microenvironment.

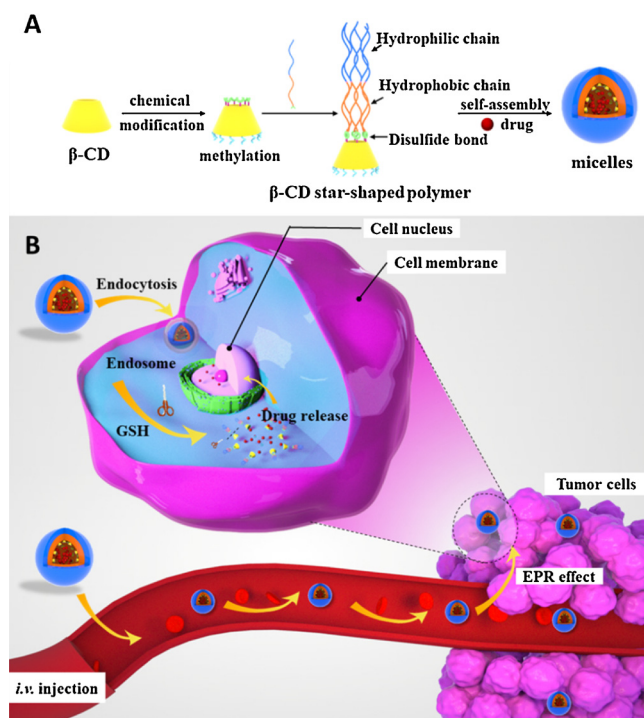


Fig. 1. Detailed synthetic routes of a series of CCPP and CPP copolymers.

polymer solutions were dialysed for 48 h, and freeze-dried into the powder form. Further details are included in the Supporting Information.

Infrared spectra of the samples were obtained using a Fourier transform infrared spectrometer (Nicolet, USA), and ^1H NMR spectra were recorded with a 400 or 500 MHz spectrometer (Bruker, Germany). The M_w and polydispersity of the copolymers were determined using Perkin-Elmer Series-200 gel permeation chromatograph (GPC) equipped with PLgel 5 μm Mixed 2D columns. THF was used as the eluent at a flow rate of 1 mL/min and a series of narrow polystyrene standards were used for calibrating the columns. High-resolution Transmission electron microscopy (TEM) samples were prepared by placing a drop of the sample solution in H_2O (concentration: 1 mg/mL) onto ultrathin carbon film. TEM was performed by using a JEOL 2100 F microscope (JEOL, Japan) with an accelerating voltage of 200 kV.

2.3. Preparation of DOX-loaded micelles

The blank micelles were first obtained by dissolving 50 mg of the different CCPPs or CPPs in 5 mL DMSO, and each was added dropwise into 25 mL deionized water under constant magnetic stirring. After stirring for 24 h at the ambient temperature, the solutions were dialyzed for 24 h to remove DMSO. The DOX-loaded micelles were obtained by dissolving 10 mg of the DOX-HCl in 1 mL DMSO, and 5.32 μL trimethylamine was added to neutralize HCl under constant magnetic stirring. After stirring for 24 h at the ambient temperature, the color of the solution slowly turned deep purple from the initial red. 10 mg of the different CCPPs or CPPs was added and the resulting mixtures were allowed to stir for 12 h, and each was added dropwise into 5 mL deionized water under constant magnetic stirring. After stirring for 24 h at the ambient temperature, the solutions were dialyzed for 48 h to remove DMSO. The blank and DOX-loaded micelles were lyophilized, and 1 mg of each was dissolved in 5 mL methanol and sonicated for 30 min. The absorption of the micelles at 490 nm (UV-vis spectra) was measured using a UV-2450 spectrophotometer (Shimadzu, Japan), and the weight was calculated from the calibration curve. Finally, the drug loading capacity (DLC) and encapsulation efficiency (EE) of the

micelles were calculated according to the following formula:

$$\text{DLC}(\%) = \frac{\text{weight of drug in micelles}}{\text{weight of drug loaded micelles}} \times 100\% \quad (1)$$

$$\text{EE}(\%) = \frac{\text{weight of drug in micelles}}{\text{weight of drug in feed}} \times 100\% \quad (2)$$

2.4. Measurement of critical micelle concentration

The critical micelle concentration (CMC) of the polymers were estimated using pyrene as the probe [35–37]. Pyrene solution in methanol was transferred through a series of volumetric flasks to evaporate the methanol and achieve a final concentration is 6×10^{-7} M. CCPP or CPP micelle solutions of different concentrations were added to the flasks, and the mixture was kept at 25 $^\circ\text{C}$ overnight. The fluorescence spectra were measured using the FLS920 spectrometer at the excitation wavelength of 335 nm, and emission wavelengths of 372 and 383 nm. The slits were set at 10 (excitation) and 2.5 nm (emission). The CMC was estimated as the cross-point when extrapolating the intensity ratio I_{372}/I_{383} at low and high concentration regions.

2.5. Size and zeta potential analysis of CCPP nanoparticles

The average size and the size distribution of the micelles were determined by dynamic light scattering (DLS). Briefly, CCPP or CPP micelles of different M_w were suspended in distilled water at 25 $^\circ\text{C}$ to prepare respective solutions of 0.5 mg/mL, and sonicated for 30 s. The micellar solutions were filtered through a 0.45 μm mesh, and measured using Zetasizer Nano-ZS (Malvern Instruments) equipped with a 633 nm He-Ne laser using back-scattering detection. The zeta potential of the micelles were tested in the same instrument after diluting the particle suspension in deionized water.

2.6. In vitro DOX release

DOX-loaded CCPP or CPP (10 mg) were suspended in 2 mL phosphate buffer saline (PBS, pH = 7.4) with or without 10 mM DTT, and transferred to a dialysis bag (3500 MWCO). The latter was placed in 8 mL PBS (with/without 10 mM DTT), and dialysis was carried at 37.5 $^\circ\text{C}$. One milliliter aliquots were drawn at certain time intervals, and replaced with the same volume of fresh buffer. The content of DOX in the eluents were measured in terms of absorbance (Abs) at 490 nm, and calculated as: y (Abs) = 0.0143x + 0.019 (x: $\mu\text{g}/\text{mL}$). The drug release rate from the copolymer was calculated with the following formula:

$$\text{Release rate}(\%) = \frac{m_t}{m} \times 100\%$$

where m_t (g) was the amount of DOX released at a given time, and m (g) was total amount of drug loaded.

2.7. Cell cytotoxicity assay

The cytotoxicity of CCPP-2, CPP-2, DOX@CCPP-2 and DOX@CPP-2 micelles was evaluated in the ovarian carcinoma (Skov 3) cells and human embryonic kidney cells (HEK 293 T) (Xiangya Hospital of Central South University, Changsha, China) with the CCK-8 assay. The Skov 3 and HEK 293 T cells were respectively cultured in RPMI 1640 and DMEM, both supplemented with 10% FBS and 1% penicillin/streptomycin, at 37 $^\circ\text{C}$ under 5% CO_2 . For the cytotoxicity assay, the cells were seeded into 96 well plates at the density of 5×10^3 cells/well and cultured for 24 h. After washing the cells thrice with PBS, 100 μL fresh medium containing different concentrations of blank CCPP-2 or CPP-2 (0, 50, 100, 200, 300, 500 and 1000 $\mu\text{g}/\text{mL}$) or the DOX (0, 1, 2, 3, 5, 7, 9, 12, 15, 18 $\mu\text{g}/\text{mL}$)-loaded micelles was added per well. After

culturing for another 24 h, the used culture medium was replaced with new medium. 10 μL CCK-8 was added to each well and the cells were incubated further for 2 h. The optical density (OD) of the cell suspensions at 450 nm was measured using a microplate reader (Bio-Rad, USA). The cell viability was calculated as follows:

$$\text{Cell viability (\%)} = \frac{\text{OD}_{\text{sample}} - \text{OD}_{\text{blank}}}{\text{OD}_{\text{control}} - \text{OD}_{\text{blank}}} \times 100\%$$

where sample, control and blank refers to the treated cells, the untreated cells and culture medium. Data were presented as means \pm SD (n = 6).

2.8. Hemolysis assay

The biocompatibility of the different micelles was also tested in terms of their hemolytic activity. Briefly, 5 mL sterile defibrinated sheep blood (leaf Biology, Shanghai) was diluted in 50 mL PBS and centrifuged at 500 g for 10 min. The RBCs were separated and washed several times with PBS till the supernatant turned colorless. After the last wash, a 10% (v/v) RBC suspension was prepared in PBS, and 100 μL aliquots were mixed with 100 μL of varying concentrations (0.05, 0.1, 0.2, 0.3, 0.5, and 1 mg/mL in PBS) of the micelles. PBS and 1% Triton X-100 were included as the negative and positive controls respectively. The mixtures were gently whirled and incubated for 2 h at 37 $^{\circ}\text{C}$ under 5% CO_2 , and centrifuged at 3000 rpm for 5 min. The supernatants were carefully removed, and 100 μL aliquots were transferred per well of a 96-well-plate. The hemoglobin released from the RBCs was measured at 540 nm using a microplate reader (Bio-Rad Instruments, USA), and the hemolysis ratio (HR) of the RBCs (%) was calculated as follows:

$$\text{Hemolysis (\%)} = \frac{\text{OD}_{\text{sample}} - \text{OD}_{\text{negative control}}}{\text{OD}_{\text{positive control}} - \text{OD}_{\text{negative control}}} \times 100\%$$

The experiment was performed in triplicates.

2.9. Cellular uptake assay

Skov 3 cells and HEK 293 T cells were seeded into 96-well plates at the density of 5000 cells/well, and treated with free or micelle-encapsulated DOX (1, 3, 5 and 9 $\mu\text{g}/\text{mL}$ DOX) after 24 h of culture. After another 24 h incubation, the cells were gently washed thrice with PBS, fixed with methanol, and stained with 1 $\mu\text{g}/\text{mL}$ DAPI. The intracellular localization of DOX was tracked by a fluorescence inversion microscope (Olympus IX 73, Japan).

2.10. Stimuli-responsive intracellular cargo release from the micelles

Cargo release from the amphiphilic micelles under reductive stimulation was tracked using the fluorescent probe coumarin 6 (C6). The C6-loaded micelles were prepared as the DOX-loaded micelles (see section 2.3), and the loaded amount was measured by absorption at 460 nm according to calibration curve. Glutathione (GSH) and the glutathione inhibitor L-buthionine-sulfoximine (BSO) were used as the positive and negative controls respectively. The Skov 3 cells and HEK 293 T cells were seeded into 96-well plates at the density of 5000 cells/well, and pre-treated with 250 μM BSO or 5 mM GSH 24 h later. After incubating for 12 h or 4 h, 3 $\mu\text{g}/\text{mL}$ C6@CCPP-2 or C6@CPP-2 was added, and the cells were cultured for another 1 h or 3 h, respectively. The nuclei and GSH were respectively stained with Hoechst 33,342 (C1025, Beyotime) and thioltracker (T10095, Thermo Fisher Scientific) for 30 min, and the fluorescence was tracked in real time by a High-Content Imaging system (Perkin Elmer). To quantify C6 release in terms of fluorescence intensity, the Skov 3 and HEK 293 T cells were seeded into 6-well plates at the density of 2×10^5 cells/mL and treated as described above. After 2 h, the cells containing C6-fluorescence were digested with 0.25% (w/v) trypsin and washed thrice with PBS to

prepare cell suspension, and acquired by flow cytometry.

2.11. In vivo tumor treatment

All animal experiments were strictly implemented under the guidelines approved by the Medical Laboratory Animal Management Committee of the Xiangya School of Medicine. SPF female BALB/c nude mice (18 ± 3 g, 3–4 weeks old) were purchased from Hunan SJA Laboratory Animal Co. Ltd (animal quality certificate No. 43,004,700,041,110 and approval No. SCXK 2016-0002) and housed at the Department of Laboratory Animals, Central South University. Each mouse was injected subcutaneously with 5×10^6 cells/mL Skov 3 cells in 200 μL into their flanks, and randomly divided into the untreated, DOX, DOX@CCPP-2 and DOX@CPP-2 groups (n = 6). Once the tumor grew to approximately 100 mm^3 , the mice were intravenously injected with the suitable vehicle at the DOX or DOX-equivalent dose of 3 mg/kg every two days. The untreated control mice received 0.5 mL/kg of saline. The tumor dimensions and the body weight of mice were measured prior to every injection. The tumor volume (mm^3) was calculated as $ab^2/2$, where a (mm) and b (mm) were respectively the longest and shortest diameters.

2.12. In vivo distribution of CCPP-2 and CPP-2 micelles

Dir-loaded micelles were prepared via a similar protocol as described in section 2.3, and used to track the systemic distribution of the micelles. Two tumor-bearing mice were respectively injected with 100 μL Dir@CCPP-2 and Dir@CPP-2 (Dir dose of 10 $\mu\text{g}/\text{mL}$) via their tail veins. The mice were imaged at 4, 12, 24 and 36 h after injection with the IVIS Lumina II multispectral imaging system (Caliper, USA), and sacrificed after the final imaging. Their vital organs (heart, liver, spleen, lung, kidney) and tumors were extracted and imaged *ex vivo* to evaluate *in situ* micellar accumulation.

To track the distribution of DOX in the tumor tissues and organs, the differentially-treated mice (see section 2.11) were sacrificed four weeks after treatment. The tumors and vital organs were weighed and homogenized, and the amount of DOX in the homogenates was extracted by CHCl_3 . After vacuum evaporation of CHCl_3 , the DOX was redissolved in chromatographic grade methanol and filtered through a 0.45 μm ultrafiltration membrane, the concentration of DOX in the tissue fluid was determined by high performance liquid chromatography (HPLC; Agilent 1260, USA). The mobile phase consisted of 0.01 M KH_2PO_4 , acetonitrile and acetic acid in the ratio of 45: 55: 0.27 (V: V: V), the flow rate was 1 mL/min and detection wavelength was 490 nm. The column used was Agilent-SB-C18 measuring 4.6×150 mm and the packing particle size was 5 μm .

2.13. Histological examination and TUNEL assay

The mice were sacrificed on the 26th day post treatment, and the tumors and major organs (heart, liver, spleen, lung and kidney) were harvested, and fixed in 4% paraformaldehyde. The fixed specimens were dehydrated, embedded in paraffin and cut into 5 μm -thick slices. The sections were deparaffinized and stained with hematoxylin and eosin (H&E) as per standard protocols, and observed under a light microscope. The apoptosis cells were detected using a TUNEL *in situ* Cell Death Detection Kit according to the manufacturer's instructions. Briefly, the sections were deparaffinized, rehydrated and treated with proteinase K for 15 min at room temperature, followed by incubation with a TUNEL mixture at room temperature for 2 h. After counterstaining with DAPI, the sections were observed with an inverted fluorescence microscope.

3. Results and discussion

3.1. Synthesis and characterization of CCPP and CPP

The synthetic routes of CCPP and CPP are illustrated in Fig. 1. The compounds 1–8 were characterized by ^1H NMR spectroscopy and FT-IR. As shown in Fig. S2 and Fig. S3, two new peaks of the ^1H NMR spectrum appeared at 0.01 and 0.84 ppm, and the peak at 4.46 ppm disappeared, indicating that the primary hydroxyl groups of β -CD were modified by tert-butyl dimethylsilyl. For compound 2, two new peaks appeared at 3.49 ppm and 3.65 ppm (Fig. S4), corresponding to the methyl group of methyl iodide. Furthermore, the peaks at 5.75 ppm disappeared, corresponding to the modification of the second hydroxyl groups. The disappearance of the peaks at 0.01 ppm and at 0.84 ppm indicated synthesis of compound 3 (Fig. S5), and the appearance of a peak at 1.59–1.67 ppm corresponding to -SH confirmed replacement of the bromide group with thiol to form compound 4 (Fig. S6). The formation of compound 5 was indicated by an intense signal corresponding to PEG at 3.64 ppm, four signals corresponding to PCL at 1.33–1.42 ppm, 1.61–1.68 ppm, 2.29–2.33 ppm and 4.04–4.08 ppm, and the disappearance of the thiol signal at 1.59–1.67 ppm (Fig. S16–S18). Compound 5 included the polymer series 2,3-OCH₃- β -CD-(SS-PCL^x-mPEG^{2k})₇, where $x = 2k, 2.5k$ and $3k$, of increasing molecular weights (according to GPC traces shown in Fig. S25A), PCL chain length and hydrophobic/hydrophilic ratios, and were accordingly designated as CCPP-1, CCPP-2 and CCPP-3. The formation of compound 6 by the iodination of the primary hydroxyl groups of β -CD was indicated by the disappearance of the peak at 4.46 ppm (Fig. S20), while the appearance of a new peak at 2.13 ppm confirmed the replacement of iodide with thiol to form compound 7 (Fig. S21). Finally, as shown in Fig. S22–S24, synthesis of compound 8 was validated by the appearance of signals corresponding to PEG and PCL (see above), and disappearance of the thiol signal at 2.13 ppm. Compound 8 included the amphiphilic polymers β -CD-(SS-PCL^x-mPEG^{2k})₇, where $x = 2k, 2.5k$ and $3k$, with controllable hydrophobic/hydrophilic ratios and were designated CPP-1, CPP-2 and CPP-3 depending on the length of PCL chains. As with the CCPP series, GPC traces (Fig. S25B) showed increasing molecular weight from CPP-1 to CPP-3.

The FT-IR spectra of the β -CD and PEG/PCL compound series are shown in Fig. S26. The appearance of a new peak at 2565 cm^{-1} ($\nu_{\text{S-H}}$ for β -CD-(SH)₇) (Fig. S26A (c)) indicated sulfhydrylation of the primary hydroxyls of β -CD, while the peaks at 1467 cm^{-1} ($\nu_{\text{C-H}}$ for -C(CH₃)₃) and 1360 cm^{-1} ($\nu_{\text{C-H}}$ for Si-(CH₃)₂) indicated tert-butyl dimethylsilyl capping (Fig. S26B (b)). The enhanced peak at 2840 cm^{-1} ($\nu_{\text{C-H}}$ for -OCH₃) corresponded to methylation (Fig. S26B (c)), and the disappearance of the peak at 1255 cm^{-1} after bromination (Fig. S26B (d)) validated (CH₃O)₁₄- β -CD-Br₇ synthesis. Finally, a new peak at 2720 cm^{-1} ($\nu_{\text{S-H}}$ for (CH₃O)₁₄- β -CD-(SH)₇) (Fig. S26B (e)) was indicative of (CH₃O)₁₄- β -CD-(SH)₇ synthesis. New peaks at 2945 cm^{-1} ($\nu_{\text{C-H}}$ for PCL), 2866 cm^{-1} ($\nu_{\text{C-H}}$ for mPEG) and 1720 cm^{-1} ($\nu_{\text{C=O}}$ for PCL) respectively corresponded to PCL and mPEG (Fig. S26C (a) and C (b)), absence of a peak at 3437 cm^{-1} ($\nu_{\text{O-H}}$ for mPEG-b-PCL) (Fig. S26C (c)) indicated removal of the hydroxyl of mPEG-b-PCL by DTPA (Fig. S26C (d)), and appearance of a peak at 2170 cm^{-1} ($\nu_{\text{S-H}}$ for mPEG^{2k}-b-PCL^{2.5k}-SH) (Fig. S26C (e)) indicated reduction of mPEG-b-PCL-DTPA by DTT. The FT-IR spectra of β -CD-(SH)₇, (CH₃O)₁₄- β -CD-(SH)₇ and mPEG^{2k}-b-PCL^{2.5k}-SH are shown in Fig. S26D (a), (b) and (c). The peak at 2565 cm^{-1} ($\nu_{\text{S-H}}$ for β -CD-(SH)₇) and 2170 cm^{-1} ($\nu_{\text{S-H}}$ for mPEG^{2k}-b-PCL^{2.5k}-SH) disappeared and new ones appeared at 2942 cm^{-1} ($\nu_{\text{C-H}}$ for PCL), 2885 cm^{-1} ($\nu_{\text{C-H}}$ for mPEG) and 1730 cm^{-1} ($\nu_{\text{C=O}}$ for PCL) upon oxidation (Fig. S26D (d) and (e)). These results suggested that mPEG^{2k}-b-PCL^{2.5k} was grafted onto β -CD through a disulfide bond. The FT-IR spectra of the remaining two amphiphilic block copolymers are shown in the Fig. S27.

3.2. Micelle formation and size distribution

Since amphiphilic block copolymers are known to form core-shell structure nanospheres with micellar properties [38], we hypothesized similar characteristics of the CCPP and CPP copolymers. As shown in Table S1, the CMCs of CCPP-1, 2 and 3 were respectively 0.0296 mg/mL, 0.0147 mg/mL and 0.0092 mg/mL, and that of CPP-1, 2 and 3 were 0.0244 mg/mL, 0.0143 mg/mL and 0.0094 mg/mL respectively. Therefore, CMC values decreased with increasing M_w of PCL, indicating that longer hydrophobic chains eased formation of amphiphilic micelles. Furthermore, the nano-micelles formed with lower concentration of the copolymers would have increased stability in circulation. We tested micelle formation by the amphiphilic CCPP-2 and CPP-2 copolymers and the hydrophilic mPEG shell by ^1H -NMR. As shown in Fig. S28 and S29, the PCL peaks disappeared in D₂O solution while that of mPEG remained visible, indicating that both copolymers assemble into core-shell type nanospheres in water.

The size of the blank and DOX-loaded micelles ranged between 80 and 135 nm (Table S2). Not surprisingly, the DOX-loaded micelles were larger than the corresponding blank micelles, indicating DOX entrapment in the hydrophobic inner cavity. To further validate DOX encapsulation in the micelles, we analyzed the ^1H -NMR spectrum of DOX@CCPP-2 micelles in D₂O (Fig. S30). Compared to the well-defined peaks of free DOX in D₂O (Fig. S30 (a)), DOX@CCPP-2 micelles lacked signals for both DOX and PCL (Fig. S30 (c)), indicating their restricted movement within the micellar core. Similar results were obtained for DOX@CPP-2 (Fig. S31). Furthermore, the blank CCPP-2 and CPP-2 micelles had regular spherical morphology typical of hollow core-shell structures, as shown in the TEM micrographs in Fig. 2A and B. The size of the nanoparticles were ~50–70 nm, making them suitable carriers for hydrophobic drugs. In contrast, the DOX-loaded micelles had a more “solid” appearance, indicating DOX encapsulation in the cavity (Fig. 2C and D). The size of these loaded particles were ~80–100 nm, which was consistent with the DLS measurements (Fig. S32). After storage for 7 days, the DLS results (Fig. S33) showed that DOX@CCPP-2 and DOX@CPP-2 in PBS had diameter of about 138 and 128 nm, respectively. Compared to the previous DLS results of DOX@CCPP-2 and DOX@CPP-2, they had no obvious change, which proved their good stability to some extent. Finally, as shown in Fig. S34, the energy spectra of CCPP-2 and CPP-2 also indicated micelle synthesis. Taken together, both CCPP-2 and CPP-2 can self-assemble in water and encapsulate DOX in the hydrophobic pocket.

3.3. Assessment of drug loading capacity and entrapment efficiency

The drug loading capacity (LC) and encapsulation efficiency (EE) of the amphiphilic micelles were further assessed by UV–vis absorption. The DOX-loaded micelles showed significantly higher absorption at 490 nm compared to the respective blank micelles (Fig. S35A and Fig. S35C). The capsulation of DOX in the hydrophobic cavity of CCPP-2 and CPP-2 micelles was also exhibited by the slight red shift in their respective strongest absorption peaks compared to free DOX in water. The drug loading behavior of the different micelles is summarized in Table S1. CCPP-2 exhibited significantly higher EE and LC (83.9% and 31.9%) compared to CCPP-1 (62.4% and 25.4%) and CCPP-3 (71.9% and 29.7%), indicating that the hydrophilic/hydrophobic ratio in the amphiphilic β -CD block copolymer is a determining factor for high LC and EE. Similarly, CPP-2 also showed higher EE and LC (76.6% and 28.6%) relative to CPP-1 (58.6% and 22.5%) and CPP-3 (68.7% and 26.8%). Therefore, the subsequent experiments were performed using CCPP-2 and CPP-2.

3.4. DOX release behavior in vitro

To demonstrate DOX release from the micelles under a reductive stimulus, we compared the amount of free DOX in PBS (pH 7.4) and in

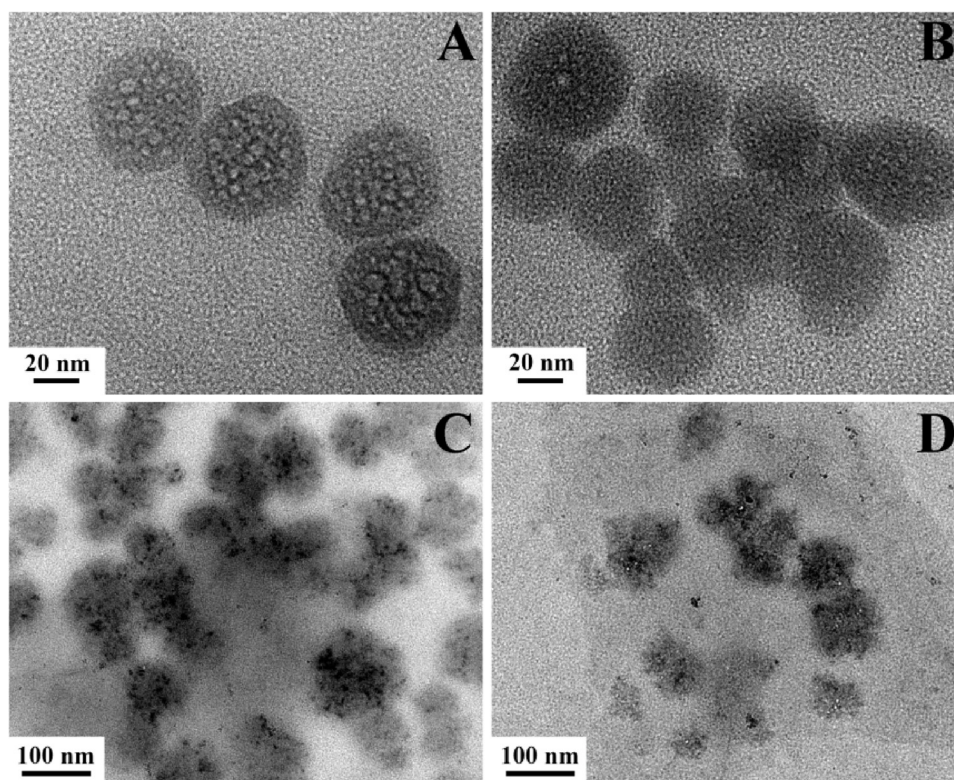


Fig. 2. TEM images of (A) CCPP-2, (B) CPP-2, (C) DOX@CCPP-2 and (D) DOX@CPP-2.

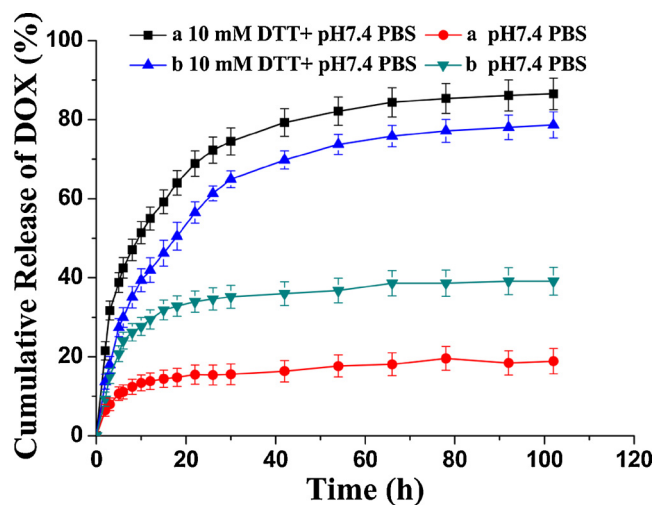


Fig. 3. DOX release curves under normal and reductive conditions from different micelles. Black square- DOX@CCPP-2 in 10 mM DTT; red circle- DOX@CCPP-2 in PBS; blue triangle-DOX@CPP-2 in 10 mM DTT; teal inverted triangle-DOX@CPP-2 in PBS.

DTT solution which simulated the reductive tumor microenvironment. As shown in Fig. S36, DOX@CCPP-2 exhibited excellent release performance under reductive stimulus comparing to the other two drug carriers. Drug burst and lag release were not observed in the DOX@CCPP-2. In contrast, the other two drug systems more or less exposed weaknesses. While DOX@CPP-2 showed similar to the result of DOX@CCPP-2 in comparison with DOX@CPP-1 and DOX@CPP-3 systems. In addition, DOX was released significantly faster from CCPP-2 in the presence of DTT than in its absence, and the cumulative release rate of DOX@CCPP-2 in DTT solution was > 50% within 8 h. In contrast, the cumulative release rate in PBS was < 20% even after 100 h (Fig. 3). This could be due to the fact that disulfide bonds are relatively stable

under physiological conditions, but rapidly break under reducing conditions which then accelerates CCPP-2 dissociation. While DOX@CPP-2 showed similar cumulative release rate in DTT, that in PBS was higher compared to DOX@CCPP-2 under the same conditions. This could be due to drug leakage from the DOX@CPP-2 micelles in physiological conditions. Taken together, DOX@CCPP-2 displayed faster drug release in the reductive environment, and no leakage under simulated physiological conditions.

3.5. *In vitro* biocompatibility and hemolytic effect of the micelles

HEK 293 T cells and Skov 3 cells were incubated with different concentrations of CPP-2 or CCPP-2 for 24 h, and the proportion of viable cells were analyzed. As shown in Fig. 4A, more than 88% of the cells survived even in the presence of 1 mg/mL of the micelles, indicating excellent biocompatibility of the nanoparticles. In addition, hemolysis assay was also performed to determine any potential detrimental effects of the copolymers on RBCs. As shown in Fig. 4B, the percentage of hemoglobin release did not exceed 2% in the presence of either the blank or DOX-loaded micelles. CCPP-2 and DOX@CCPP-2 showed < 1% hemolysis rate, even at the maximum concentration of 1 mg/mL, far below the international standard (5%), further validating their good biocompatibility.

3.6. Cell uptake of the copolymer micelles

The cellular uptake of CCPP-2 and CPP-2 nanoparticles was tracked by loading the fluorescent probe-C6 into the micellar cavity. In addition, the cells were also labeled with a thiol-tracker to detect disulfide bond breakage in GSH and/or the mercapto groups on β -CD. As shown in Fig. 5A, Skov 3 cells treated with C6@CCPP-2 or C6@CPP-2 showed dual fluorescence, which enhanced significantly in the presence of GSH in a concentration-dependent manner, indicating effective C6 release. Addition of the GSH inhibitor BSO significantly weakened the fluorescence intensity of both probes, indicating that cargo release from these

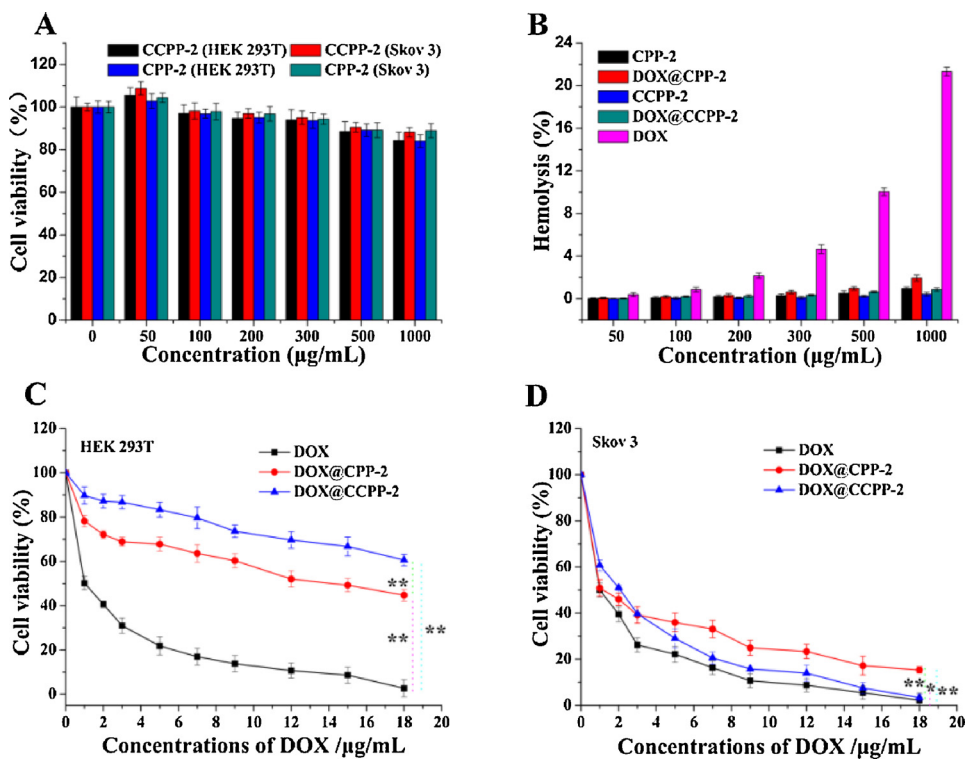


Fig. 4. (A) Viability of the HEK 293 T and Skov 3 cells incubated with varying concentrations of CCPP-2 and CPP-2 for 24 h. (B) Hemolysis rate of CPP-2, DOX@CPP-2, CCPP-2, DOX@CCPP-2 and DOX. (C–D) Viability of (C) HEK 293 T and (D) Skov 3 cells incubated with varying concentrations of DOX, DOX@CPP-2 and DOX@CCPP-2 for 24 h. * $p < 0.05$, ** $p < 0.01$.

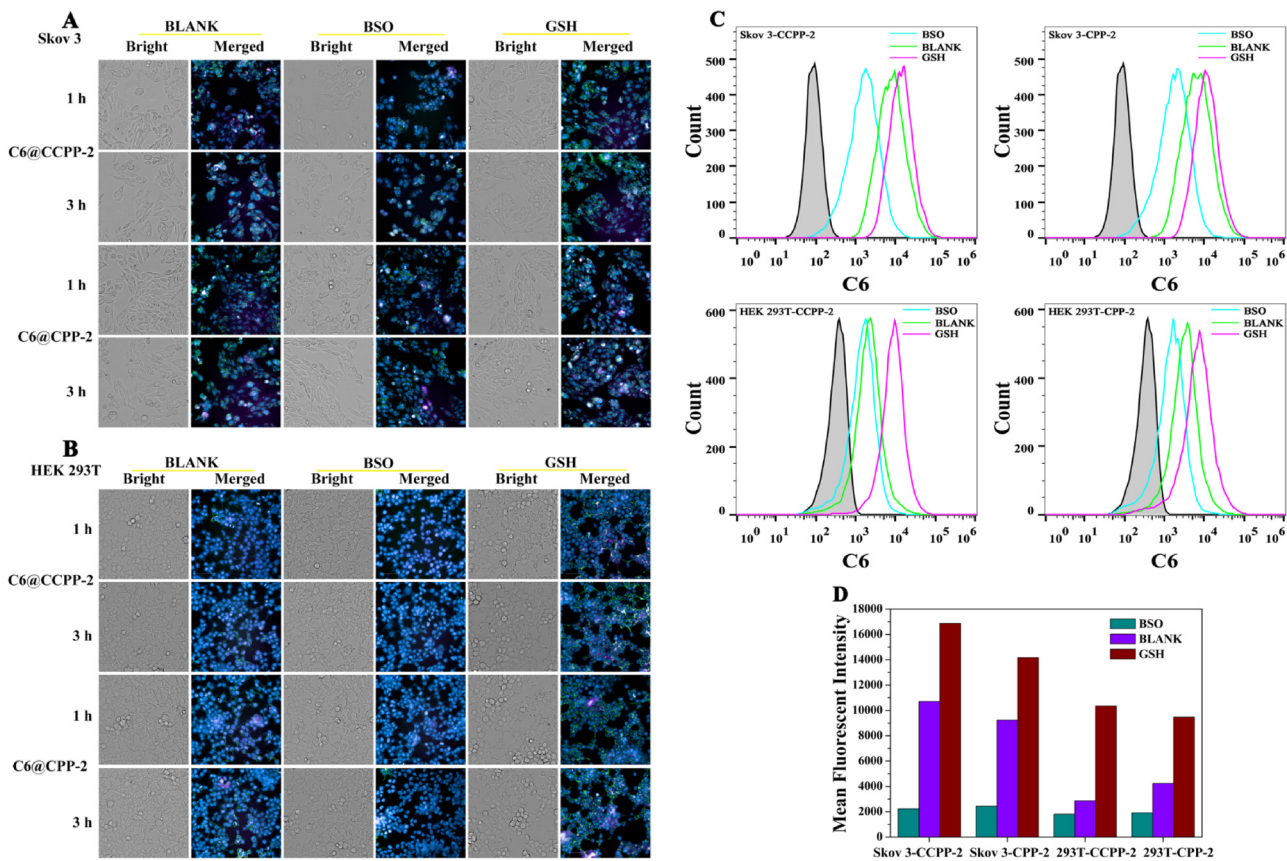


Fig. 5. (A–B) Representative fluorescence images of (A) Skov 3 and (B) HEK 293 T cells after incubation with C6@CCPP-2 and C6@CPP-2 for 1 h and 3 h. (C) Representative flow cytometric histograms showing the cellular uptake of C6@CCPP-2 and C6@CPP-2 in Skov 3 and HEK 293 T cells. (D) Mean fluorescence intensity of Skov 3 and HEK 293 T cells treated with C6@CCPP-2 and C6@CPP-2.

micelles requires a reductive environment which breaks the disulfide linkages and disintegrates the micelles. Furthermore, the fluorescence intensity of cells incubated with C6@CCPP-2 was less compared to the C6@CPP-2-treated cells in the absence of GSH, which indicated minimal leakage of C6 from the CCPP-2 micelles under normal conditions. In contrast to the Skov 3 cells, the non-transformed HEK 293 T cells treated with C6@CCPP-2 or C6@CPP-2 fluoresced weakly even in the presence of GSH (Fig. 5B), signifying the cancer cell-specificity of these micellar carriers. Similar results were obtained with flow cytometry analysis, both in terms of the percentage of fluorescently labeled cells and the mean fluorescence intensity (MFI) (Fig. 5C and 5D). Taken together, the amphiphilic copolymer micelles are highly effective drug carriers that can selectively release the cargo in cancer cells, and CCPP-2 in particular can achieve controlled drug release in the reductive tumor microenvironment, thereby minimizing drug leakage in circulation.

3.7. Anticancer effects of the DOX carriers *in vitro*

To further assess the specific anticancer effects of DOX@CCPP-2 and DOX@CPP-2, we evaluated their toxicity in both HEK 293 T cells and Skov 3 cells. As shown in Fig. 4C and Fig. 4D, the half maximal inhibitory concentration (IC_{50}) of free DOX in HEK 293 T cells and Skov 3 cells were $0.9 \mu\text{g/mL}$ and $1 \mu\text{g/mL}$, respectively, which points to indiscriminate toxicity in both malignant and normal cells. In contrast, the encapsulated DOX exhibited minimal toxicity in the HEK 293 T cells, while maintaining a strong killing effect on the Skov 3 cells. The IC_{50} values of DOX@CCPP-2 and DOX@CPP-2 loaded with equivalent amount of DOX ($5 \mu\text{g/mL}$) were respectively $2 \mu\text{g/mL}$ and $1 \mu\text{g/mL}$ in Skov 3 cells, and over $18 \mu\text{g/mL}$ and $14 \mu\text{g/mL}$ in HEK 293 T cells. Since the GSH content in the Skov 3 cells is 1000 times higher compared to that in 293 T cells, the disulfide bonds of the drug-loaded nanoparticles are sensitive to breakage in the reductive environment of these cells. Consistent with the IC_{50} values, the survival rate of Skov 3 cells and HEK 293 T cells treated with DOX@CCPP-2 was 29% and 83% respectively, and 36% and 67% after treatment with DOX@CPP-2. Therefore, DOX@CCPP-2 was selectively toxic towards Skov 3 cells without significantly effecting HEK 293 T cells. In contrast, premature DOX leakage from DOX@CPP-2 lowered its efficacy against the cancer cell line, but resulted in increased toxicity to the non-transformed cells. Furthermore, Skov 3 cells treated with DOX@CCPP-2, DOX@CPP-2 and DOX for 24 h showed varying degrees of nuclear damage (Fig. S37A, C, E), while only free DOX and DOX@CPP-2 resulted in nuclear deformation in the HEK 293 T cells (Fig. S37D, F), DOX@CCPP-2 exhibited low cytotoxicity towards HEK 293 T cells (Fig. S37B). Taken together, DOX@CCPP-2 combines superior anticancer efficacy and negligible cytotoxicity, on account of high drug load capacity, stimulus-responsive drug release, low leakage and appropriate particle size.

3.8. *In vivo* distribution of the drug-loaded micelles

To track the *in vivo* distribution of the micelles, mice were injected intravenously with Dir@CCPP-2 or Dir@CPP-2, and imaged 4, 12, 24 and 36 h later using the IVIS Lumina II multispectral imaging system. In addition, the tumors and major tissues were dissected and photographed after 36 h using this imaging system. As shown in Fig. 6, both Dir@CCPP-2 and Dir@CPP-2 accumulated at the tumor sites in a time-dependent manner, likely due to the EPR effect, and showed controlled release in the tumor tissues. However, Dir@CPP-2 was also noticeable in the normal organs due to its leakage in the circulation. In addition, the *ex vivo* images of the tumors and other tissues of the Dir@CCPP-2-treated mice showed relatively strong fluorescence signals in the liver and spleen, which could be due to the Kupffer cells in the liver and spleen macrophages. Nevertheless, the tumor tissues had 2.8-fold and 6.9-fold higher fluorescence intensity compared to the liver and spleen respectively, and very low signals were recorded in the heart, lungs and

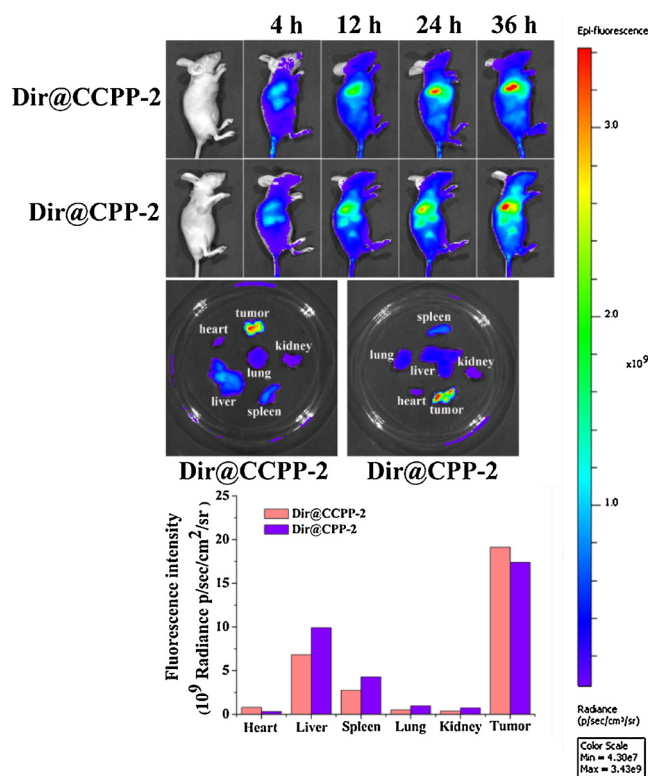


Fig. 6. Representative images showing time-dependent accumulation of Dir@CCPP-2 and Dir@CPP-2 in Skov 3 tumor-bearing mice (upper panels). Bar graphs showing fluorescence intensity of Dir in major organs and tumors after 36 h (lower panel).

kidneys. In contrast, Dir@CPP-2 showed slightly higher non-specific accumulation compared to Dir@CCPP-2, due to its poor enrichment effect as indicated in previous experiments. Taken together, the appropriate size and excellent stimulus responsiveness of Dir@CCPP-2 enabled its targeted accumulation and release in the cancer tissues, with minimal leakage to the normal tissues.

3.9. Antitumor efficacy of DOX@CCPP-2 and DOX@CPP-2 *in vivo*

The tumor-bearing mice were treated with saline, free DOX, DOX@CPP-2 or DOX@CCPP-2, and the tumor sizes and body weight were monitored regularly to assess the antitumor effects of the drug carriers *in vivo*. As shown in Fig. 7, DOX@CCPP-2 showed significantly better antitumor effect than the other groups. Although compared with saline group, the other three groups could significantly inhibit the increase of tumor volume. DOX@CCPP-2 had better efficacy because of the EPR effect when compared with free DOX group. Fig. 7A, B showed representative photograph images of tumor-bearing mice and excised tumors after injection of saline, DOX, DOX@CPP-2 and DOX@CCPP-2, respectively. The represent mice photos reflected the change of tumor size and the tumor morphology of each group. DOX@CCPP-2 displayed the strongest antitumor effect among all groups through visual observation. The mice treated with saline (control group) exhibited rapid tumor growth tendency. However, DOX, DOX@CPP-2 and DOX@CCPP-2 treatments displayed different influences on tumors growth inhibitions when comparing with those of control groups (Fig. 7D). Interestingly, unlike the results of cell viability evaluation *in vitro*, pure DOX only displayed moderate inhibition effect on tumor growth *in vivo*. It was related to the fact that free DOX quickly permeated into all tissues of mice after intravenous injection, resulting in potential toxic side effect on normal tissues, thus only small amount of DOX could reach tumor site *in vivo*. On the other hand, free DOX had only short life time *in vivo*, and would be cleared off from the host *via* blood circulation and

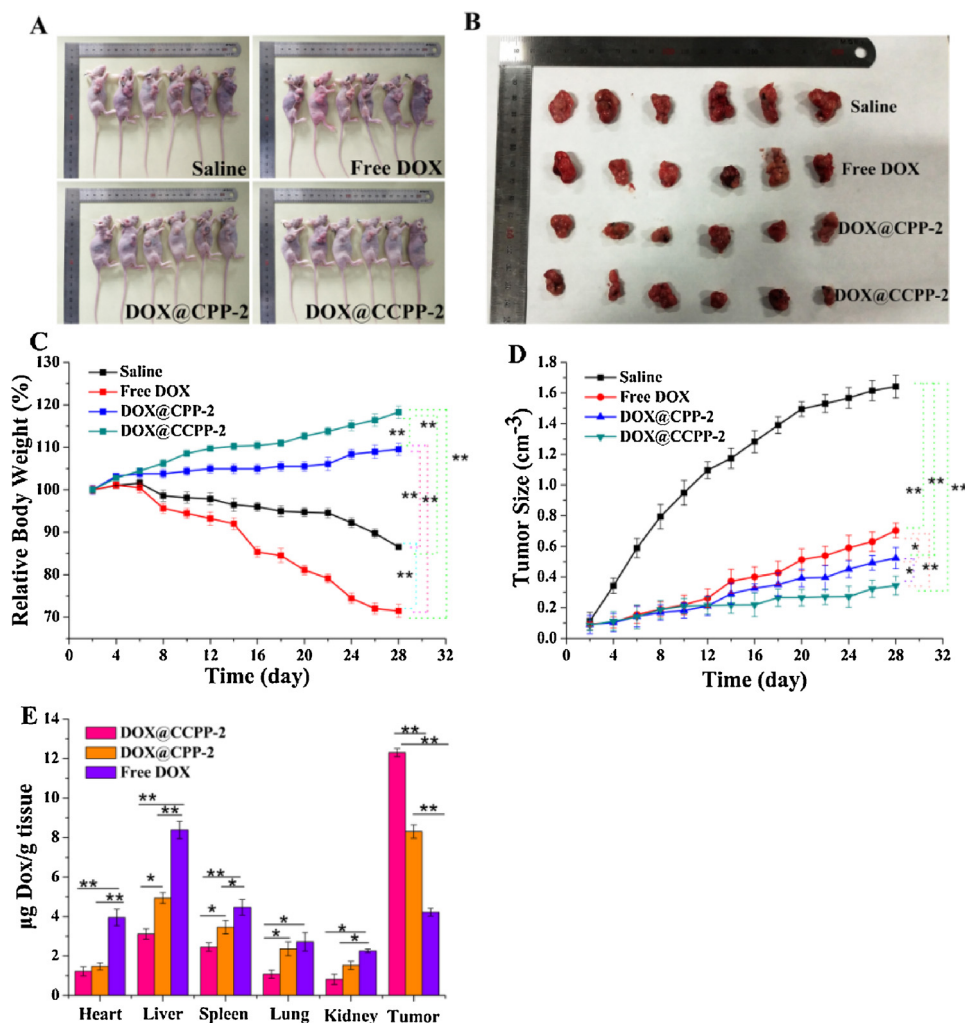


Fig. 7. (A) Representative photographs of mice after treatment with saline, DOX, DOX@CPP-2 and DOX@CCPP-2 for 26 days. (B) Body weights of the differentially-treated mice during the treatment regimen normalized to the initial values (* $P < 0.05$ and ** $P < 0.01$). (C) Representative images of the excised solid tumors after 26 days of treatment. (D) Relative tumor volume in the different groups during the treatment (* $P < 0.05$ and ** $P < 0.01$). (E) Concentration of DOX in tumor tissues and major organs after treatment (* $P < 0.05$ and ** $P < 0.01$).

metabolism. DOX@CPP-2 group showed a moderate inhibition effect on tumor growth, since CPP-2 could partially reduce DOX diffusion on its way heading for tumor site. DOX@CCPP-2 group displayed the most notable tumor growth inhibition efficiency, with significantly smaller tumor size than those of other groups. To investigate the potential tissue toxicity of DOX@CCPP-2 *in vivo*, the body weight of nude mice was also periodically monitored (Fig. 7C). For free DOX group, the mice weights started to decrease on the 4th day, indicating that DOX had severe side toxic effect on nude mice. The weight of mice in the saline group first increased and then decreased with the increase of tumor, this was due to large tumors likely interfered with normal physiological functions, resulting in weight loss. The body weights of nude mice increased with different degrees after administrations of DOX@CPP-2 and DOX@CCPP-2, respectively. The result suggested that CPP-2 and CCPP-2 have good biocompatibility *in vivo* and reduce the toxicity of DOX as nanocarriers. Taken together, DOX@CCPP-2 displayed excellent tumor clearance with low toxicity to normal tissues, on account of the EPR effect and excellent stimulus responsiveness.

3.10. Drug distribution and toxicity *in vivo*

The DOX content in the different tissues was measured by HPLC after extracting and homogenizing the tissue samples. As shown in Fig. 7E, the DOX content in the tumor tissues of the DOX@CCPP-2

group was 2.9 times greater than in the tumors of the free DOX group, and 4 times higher than that in the normal tissues. In contrast, the DOX concentration was higher in the normal organs of the free DOX-treated mice compared to the tumor tissues. Therefore, in the absence of targeted and controlled release, DOX can cause severe side effects when it enters the circulation. The potential toxic effects of DOX, DOX@CPP-2 and DOX@CCPP-2 on both normal and tumor tissues were also evaluated by HE staining (Fig. 8A). Compared to pure DOX, the encapsulated forms resulted in negligible toxicity in the heart, liver, spleen, lung and kidney, and caused significant damage in the tumor tissues. Furthermore, the TUNEL assay showed significantly higher proportion of apoptotic cells in the tumor tissues of the mice treated with DOX@CCPP-2 or DOX@CPP-2 compared to the free DOX group (Fig. 8B). In addition, DOX@CCPP-2 resulted in higher apoptosis rate compared to DOX@CPP-2. Therefore, consistent with the results so far, DOX@CCPP-2 exhibited superior anticancer performance and low toxic side effects due to its targeted accumulation and stimuli-responsive release.

4. Conclusions

We constructed a novel amphiphilic micellar drug delivery platform with a β -CD core and amphiphilic block copolymer arms, which showed high drug loading capacity, targeted uptake in cancer cells, controlled

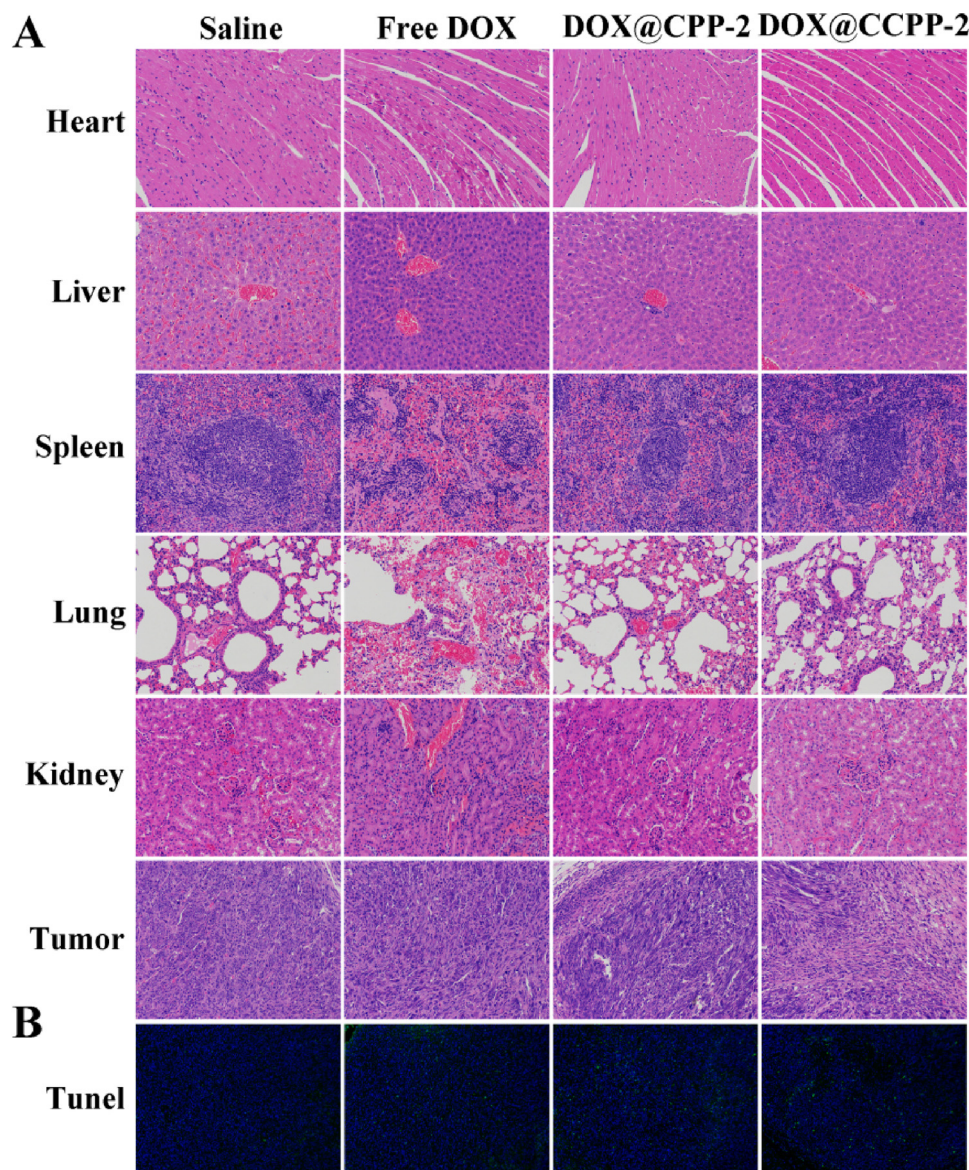


Fig. 8. (A) Representative images of H&E stained tissues of mice treated with saline, DOX, DOX@CPP-2 and DOX@CCPP-2 for 26 days. Nuclei-blue and cytoplasm-red. (B) Representative fluorescence images showing TUNEL-positive cells (green) in the tumor tissues of different treatment groups. DAPI stained nuclei-blue, scale bar = 100 μm .

drug release under reductive conditions and minimal toxic effects in normal cells. In the tumor-bearing mouse model, the DOX-loaded micelles were enriched at the tumor site *via* EPR, and resulted in significant tumor clearance with negligible effects on the healthy tissues. This is a highly promising nanovehicle for targeted anti-cancer therapy and should be further tested clinically.

Declaration of Competing Interest

The authors declare no competing interests.

Acknowledgement

This project was financially supported by the National Natural Science Foundation of China (No.21576295), the Fundamental Research Funds for the Central Universities of Central South University (2017zzts175) and the Open-End Fund for the Valuable, Precision Instruments of Central South University (CSUZC201830). We thank the MRI facility of School of Chemistry and Chemical Engineering of

Central South University for technical support.

Appendix A. Supplementary data

Supplementary material related to this article can be found, in the online version, at doi:<https://doi.org/10.1016/j.colsurfb.2019.110425>.

References

- [1] H.L. Mao, Y.D. Xie, H.C. Ju, H.S. Mao, L. Zhao, Z. Wang, L. Hua, C.M. Zhao, Y.L. Li, R.T. Yu, H.M. Liu, Design of tumor microenvironment responsive drug-drug micelle for cancer radiochemotherapy, *ACS Appl. Mater. Interfaces* 10 (2018) 33923–33935.
- [2] T.M. Sun, Y.S. Zhang, B. Pang, D.C. Hyun, M.X. Yang, Y.N. Xia, Engineered nanoparticles for drug delivery in cancer therapy, *Angew. Chem. Int. Ed.* 53 (2014) 12320–12364.
- [3] X.X. Shi, X.Q. Ma, M.L. Hou, Y.E. Gao, S. Bai, B. Xiao, P. Xue, Y.J. Kang, Z.G. Xu, C.M. Li, pH-Responsive unimolecular micelles based on amphiphilic star-like copolymer with high drug loading for effective drug delivery and cellular imaging, *J. Mater. Chem. B Mater. Biol. Med.* 5 (2017) 6847–6859.
- [4] C.X. Yan, Z.Q. Guo, Y.Y. Shen, Y. Chen, H. Tian, W.H. Zhu, Molecularly precise self-assembly of theranostic nanoprobes within a single-molecular framework for *in vivo*

- tracking of tumor-specific chemotherapy, *Chem. Sci.* 9 (2018) 4959–4969.
- [5] H.Y. Xu, P.M. Yang, H.F. Ma, W.D. Yin, X.X. Wu, H. Wang, D.M. Xu, Z. Xia, Amphiphilic block copolymers-based mixed micelles for noninvasive drug delivery, *Drug Deliv.* 23 (2016) 3063–3071.
- [6] X.L. Wei, Y.G. Wang, W.F. Zeng, F. Huang, L. Qin, C.L. Zhang, W. Liang, Stability influences the biodistribution, toxicity, and anti-tumor activity of doxorubicin encapsulated in PEG-PE micelles in mice, *Pharm. Res.* 29 (2012) 1977–1989.
- [7] N. Nishiyama, K. Kataoka, Nanostructured devices based on block copolymer assemblies for drug delivery: designing structures for enhanced drug function, *Adv. Polym. Sci.* 193 (2006) 67–101.
- [8] S. Zeng, M.P. Xiong, Trilayer micelles for combination delivery of rapamycin and siRNA targeting Y-box binding protein-1 (siYB-1), *Biomaterials* 34 (2013) 6882–6892.
- [9] J.Q. Yan, T. Su, F.R. Cheng, J. Cao, H. Zhang, B. He, Multifunctional nanoparticles self-assembled from polyethylenimine-based graft polymers as efficient anticancer drug delivery, *Colloids Surf. B Biointerfaces* 155 (2017) 118–127.
- [10] D. Sutton, S.H. Wang, N. Nasongkla, J.M. Gao, E.E. Dormidontova, Doxorubicin and beta-lapachone release and interaction with micellar core materials: experiment and modeling, *Exp. Biol. Med.* 232 (2007) 1090–1099.
- [11] T. Noh, Y.H. Kook, C. Park, H. Youn, H. Kim, E.T. Oh, E.K. Choi, H.J. Park, C. Kim, Block copolymer micelles conjugated with anti-EGFR antibody for targeted delivery of anticancer drug, *J. Polym. Sci. Part A: Polym. Chem.* 46 (2008) 7321–7331.
- [12] G.B. Hong, R.X. Yuan, B.L. Liang, J. Shen, X.Q. Yang, X.T. Shuai, Folate-functionalized polymeric micelle as hepatic carcinoma-targeted, MRI-ultrasensitive delivery system of antitumor drugs, *Biomed. Microdevices* 10 (2008) 693–700.
- [13] X.T. Shuai, H. Ai, N. Nasongkla, S. Kim, J.M. Gao, Micellar carriers based on block copolymers of poly(ϵ -caprolactone) and poly(ethylene glycol) for doxorubicin delivery, *J. Control. Release* 98 (2004) 415–426.
- [14] N.V. Cuong, M.F. Hsieh, Y.T. Chen, I. Liau, Synthesis and Characterization of PEG-PCL-PEG Triblock Copolymers as Carriers of Doxorubicin for the Treatment of Breast Cancer, *J. Appl. Polym. Sci.* 117 (2010) 3694–3703.
- [15] Y.Y. Zhou, L. Li, W. Chen, D. Li, N.C. Zhou, J.L. He, P.H. Ni, Z.B. Zhang, X.L. Zhu, A twin-tailed tadpole-shaped amphiphilic copolymer of poly(ethylene glycol) and cyclic poly(ϵ -caprolactone): synthesis, Self-assembly and Biomedical Application, *Polym. Chem.* 9 (2018) 4343–4353.
- [16] A.A. Christy, Water adsorption properties of free and dehydrated β -Cyclodextrin studied by near infrared spectroscopy and gravimetry, *Key Eng. Mater.* 689 (2016) 143–147.
- [17] L.Y. Hu, J.F. Han, W.Q. Qiao, X.K. Zhou, C.L. Wang, D.G. Ma, Y.N. Li, Z.Y. Wang, Side-chain engineering in naphthalenediimide-based n-type polymers for high-performance all-polymer photodetectors, *Polym. Chem.* 9 (2018) 327–334.
- [18] V.R. Yadav, S. Prasad, R. Kannappan, J. Ravindran, M.M. Chaturvedi, L. Vaahtera, J. Parkkinen, B. Aggarwal, Cyclodextrin-complexed curcumin exhibits anti-inflammatory and antiproliferative activities superior to those of curcumin through higher cellular uptake, *Biochem. Pharmacol.* 80 (2010) 1021–1032.
- [19] M. Sivasubramanian, T. Thambi, V.G. Deepagan, G. Saravanakumar, H. Ko, Y.M. Kang, J.H. Park, Carboxymethyl dextran-cyclodextrin conjugate as the carrier of doxorubicin, *J. Nanosci. Nanotechnol.* 13 (2013) 7271–7278.
- [20] L. Szente, J. Szejtli, Highly soluble cyclodextrin derivatives: chemistry, properties, and trends in development, *Adv. Drug Deliver. Rev.* 36 (1999) 17–28.
- [21] S. Aquino, N. Quach, C. Richardson, C. McDonald, The potential use of cyclodextrins in parenteral formulations, *J. Parenter. Sci. Technol.* 44 (1990) 48–49.
- [22] J.A. Yáñez, M.L. Forrest, Y. Ohgami, G.S. Kwon, N.M. Davies, Pharmacometrics and delivery of novel nanoformulated PEG-b-poly(ϵ -caprolactone) micelles of rapamycin, *Cancer Chemother. Pharmacol.* 61 (2008) 133–144.
- [23] F. Liu, A. John, Y. Li, H. Majeed, R. Liang, Y. Ma, J.G. Ma, F. Zhong, Chitosan/sulfobutylether- β -cyclodextrin nanoparticles as a potential approach for tea polyphenol encapsulation, *Food Hydrocoll.* 57 (2016) 291–300.
- [24] L. Liu, C.X. Li, X.C. Li, Z. Yuan, Y.L. An, B.L. He, Biodegradable polylactide/poly(ethylene glycol)/polylactide triblock copolymer micelles as anticancer drug carriers, *J. Appl. Polym. Sci.* 80 (2010) 1976–1982.
- [25] E. Pierri, K. Avgoustakis, Poly(Lactide)-Poly(Ethylene glycol) micelles as a carrier for griseofulvin, *J. Biomed. Mater. Res. Part B Appl. Biomater.* 75 (2005) 639–647.
- [26] J. Szeman, H. Ueda, J. Szejtli, E. Fenyvesi, Y. Machida, T. Nagai, Complexation of several drugs with water-soluble cyclodextrin polymer, *Chem. Pharm. Bull.* 35 (1987) 282–288.
- [27] L. Zhang, J.F. Lu, Y.M. Jin, L.Y. Qiu, Folate-conjugated beta-cyclodextrin-based polymeric micelles with enhanced doxorubicin antitumor efficacy, *Colloids Surf. B Biointerfaces* 122 (2014) 260–269.
- [28] J.S. Li, Z.Q. Guo, J.Y. Xin, G.L. Zhao, H.N. Xiao, 21-Arm star polymers with different cationic groups based on cyclodextrin core for DNA delivery, *Carbohydr. Polym.* 79 (2010) 277–283.
- [29] S. Mura, J. Nicolas, P. Couvreur, Stimuli-responsive nanocarriers for drug delivery, *Nat. Mater.* 12 (2013) 991–1003.
- [30] Y. Yang, L.G. Xu, W.J. Zhu, L.Z. Feng, J.J. Liu, Q. Chen, Z.L. Dong, J.X. Zhao, M.Y. Chen, One-pot synthesis of pH-responsive charge-switchable PEGylated nanoscale coordination polymers for improved cancer therapy, *Biomaterials* 156 (2018) 121–133.
- [31] C. Hegedűs, K. Kovács, Z. Polgár, Z. Regdon, É. Szabó, A. Robaszekiewicz, H. JayForman, A. Martner, L. Virág, Redox control of cancer cell destruction, *Redox Biol.* 16 (2018) 59–74.
- [32] C.L. Sun, X.Y. Li, X.D. Du, T. Wang, Redox-responsive micelles for triggered drug delivery and effective laryngopharyngeal cancer therapy, *Int. J. Biol. Macromol.* 112 (2018) 65–73.
- [33] M. De Smet, S. Langereis, S.V. Den Bosch, H. Grull, Temperature-sensitive liposomes for doxorubicin delivery under MRI guidance, *J. Control. Release* 143 (2010) 120–127.
- [34] X.S. Meng, B. Gui, D.Q. Yuan, M. Zeller, C. Wang, Mechanized azobenzene-functionalized zirconium metal-organic framework for on-command cargo release, *Sci. Adv.* 2 (2016) e1600480.
- [35] C.Y. Chen, T.H. Kim, W.C. Wu, C.M. Huang, H. Wei, C.W. Mount, Y.Q. Tian, S.H. Jang, S.H. Pun, A.K.Y. Jen, pH-dependent, thermosensitive polymeric nanocarriers for drug delivery to solid tumors, *Biomaterials* 34 (2013) 4501–4509.
- [36] Q. Zhao, T.T. Pan, G. Xiang, Z.P. Mei, J.P. Jiang, G. Li, X.S. Zou, M.W. Chen, D.Z. Sun, S.M. Jiang, Y.Q. Tian, Highly efficient ratiometric extracellular oxygen sensors through physical incorporation of a conjugated polymer and PtTFPP in graft copolymers, *Sens. Actuators B Chem.* 273 (2018) 242–252.
- [37] W.D. Ke, W. Yin, Z.S. Zha, J.F. Mukerabigwi, W.J. Chen, Y.H. Wang, C.X. He, Z.S. Ge, A robust strategy for preparation of sequential stimuli-responsive block copolymer prodrugs via thiolactone chemistry to overcome multiple anticancer drug delivery barriers, *Biomaterials* 154 (2018) 261–274.
- [38] G.S. Kwon, M. Naito, M. Yokoyama, T. Okano, Y. Sakurai, K. Kataoka, Physical entrapment of adriamycin in AB block copolymer micelles, *Pharm. Res.* 12 (1995) 192–195.